J. Space Weather Space Clim. 2026, **16**, 25
© T.A. Stockmans et al., Published by EDP Sciences, 2026
https://doi.org/10.1051/swsc/2026022

Available online at:
www.swsc-journal.org

TECHNICAL ARTICLE

OPEN ACCESS

Conceptual design and prototyping of a three-color polarimetric imaging instrument for auroral observations

Thijs A. Stockmans[1,*], Kira Strelow[1], Naor Scheinowitz[1], Fedde Fagginger Auer[1], Willeke Mulder[1], Remko Stuik[1], Gaël Cessateur[2], Leo Bosse[2], Hervé Lamy[2], and Frans Snik[1]

[1]Leiden Observatory, Leiden University, P.O. Box 9513, 2300, RA Leiden, The Netherlands
[2]Belgium Institute for Space Aeronomy, Ringlaan-3-Avenue Circulaire, 1180 Brussels, Belgium

Received 11 December 2025 / Accepted 28 May 2026

Abstract – Measurements of the polarization of the aurora remain challenging but would enable the inference of the magnetic field's dynamics and the energetics of the impacting charged particles during geomagnetic storms. Here we present a novel three-color imaging instrument for measuring the polarization of the aurora. The instrument concept is based on a commercial micro-patterned linear polarization camera with Red-Green-Blue color filters. This detector type enables a very compact instrument concept where both the spectral selectivity and the polarization measurement is performed in a snapshot fashion by the imaging chip. We implement additional spectral filters to specifically select the wavelengths of the auroral lines and add a rotating half-wave plate to enhance the polarimetric performance. We have developed a first prototype, called PANIC (Polarization of the Aurora in the North Imaging Camera), to proof the measurement principle. The first observations during a field campaign in Skibotn (Norway) exhibit a sub-percent polarimetric sensitivity and accuracy, rendering the instrument concept viable for routine observations. We discuss future upgrades to improve the instrument stability and its capability to discern auroral signals from other light sources.

Keywords: Aurora / Polarization / Instrumentation

1 Introduction

The aurora is a manifestation of space weather that has a direct impact on our daily lives on Earth. While the aurora itself is beautiful and spectacular, the geomagnetic storms due to solar coronal mass ejections also give rise to communication disruptions, power outages, and satellite failures. To better understand and monitor the effects of such solar storms impacting our Earth, we need to measure the dynamics of the Earth's magnetic field and the energetics of the impacting electrons and protons at multiple layers of our atmosphere. Measurements in the thermosphere can be enhanced by measuring the polarization of the aurora, particularly in the red line (Lilensten et al., 2006).

Auroral emissions are the consequence of the external forcing of the solar wind on the Earth's magnetosphere. Particles from the solar wind can penetrate the Earth's magnetosphere through different processes, leading to a plasma enrichment of the Earth's magnetotail, more specifically within the plasma sheet. Closed magnetic field loops with an upper Earth latitude ionospheric footprint are connected to the plasma sheet. The magnetospheric particles in the plasma sheet are then accelerated along those geomagnetic field lines, forming the field-aligned electric currents, or Birkeland currents (Sato & Iijima, 1979). While precipitating into the ionosphere, magnetospheric electrons can excite and heat up the upper-altitude constituents of the atmosphere through collisions. The main constituents of interest above 90 km altitude are atomic oxygen and N_2. The N_2 molecule can be directly electron-impacted to form excited N_2^+, which will be excited through the molecular band emission at 427.8 nm. For the generation process of the forbidden atomic oxygen line emissions, some photochemical reactions need to be taken into account along with the electron impact process. Dissociative recombination of O_2^+ is an important production of O(1S) and O(1D) states, leading to spectral lines emissions at 557.7 nm and the triplet at 630.0, 636.4 nm, and 639.2 nm, respectively (Peverall et al., 2001). The O(1S) state can also be produced efficiently by a two-step process: first, the excitation of N_2 by electron impact, then a chemical reaction between the latter and atomic oxygen (Whiter et al., 2023). Those atomic oxygen line emissions, however, are forbidden transitions, with a significant lifetime of about 110 s for O(1D). De-excitation through collisions is therefore important and the emission can only occur due to the low density at

*Corresponding author: stockmans@strw.leidenuniv.nl

This is an Open Access article distributed under the terms of the Creative Commons Attribution License (https://creativecommons.org/licenses/by/4.0), which permits unrestricted use, distribution, and reproduction in any medium, provided the original work is properly cited.

these high altitudes. The auroral spectrum is also composed of many other spectral lines and molecular bands, such as N_2, but also H_α coming from the proton aurora (Galand & Chakrabarti, 2006). While we focus here on the three predominant emission lines because of their high intensity, we direct the reader to Rees (1989) for a more exhaustive account of all auroral lines.

The impacting electrons are directed primarily along the magnetic field lines, which causes an anisotropy in the excitation, and can therefore create an imbalance in populated Zeeman sub-levels of the excited state (Bommier et al., 2011). The spectral line resulting from de-excitation can therefore be strongly polarized. The auroral red line, as part of a triplet transition, is therefore likely to be polarized, whereas the green line, does not contain multiple Zeeman levels and, in principle, cannot be polarized. However, the fractional polarization of the red auroral line is decreased by depolarization mechanisms such as elastic collisions and mixing with other generation systems for the excited O atoms (the indirect chemical reaction pathway described above). Due to the long lifetime of the excited state, these effects can reduce the theoretically maximum linear polarization of 17% to ∼1% (Bommier et al., 2011). Nevertheless, this residual polarization signal (degree and angle of linear polarization) still contains important information on the direction and energetics of the impacting particles.

The first attempt to measure polarization in the red line was made by Harang (1933), followed by several other scientists during the decades that followed. However, none of the earlier authors succeeded in making a measurement. The first actual measurement of the polarization of the aurora came in 1959, when Duncan (1959) claimed a polarization signal of the red aurora of around 30%. However, this high number was soon discredited by Chamberlain (1959), who disputed the measurements for being too high. In that paper, he also alludes to the importance of measurements of the auroral polarization already being expressed by Ginsburg (1943), who already theorized on the absence of polarization in the 557.7 green line.

The call for more measurements was not picked up for half a century, until Lilensten et al. (2008) reported the measurement of polarization in the 630.0 line. They mention a constant degree of linear polarization (DoLP) of 6% in the sky except during auroral activity, where it reduces to 2%. Those measurements were performed with two photomultipliers, one of which carried a rotating linear polarizer. This observation was concurrently (re)interpreted by Bommier et al. (2011), who introduced a semi-classical framework to explain the polarization of the red aurora and credited the previously reported polarization of outside auroral activity by Lilensten et al. (2008) to scattered light from surrounding villages. The main argument was that the angle of linear polarization is expected to be along the incident average propagation direction of the electrons, contrary to what was found outside auroral activity, (Lilensten et al., 2008).

More measurements of the red lines at 630 nm were conducted with multiple instruments, finding signals between 1% and 7% (Barthélémy et al., 2011; Lilensten et al., 2013; Bosse et al., 2020). Interest also expanded to different lines, when measurements of the blue 427.8 nm detected polarization signals between 1% and 2%, for the purple 391.4 nm line at 5%, as well as the green 557.7 nm line polarized at a maximum of 2.5% (Barthelemy et al., 2019; Bosse et al., 2020). The polarization in the 557.7 nm line was especially surprising because of the theoretical arguments that it should not be polarized. Since measurements were not free of stray light, this was modeled in Bosse et al. (2022a). The authors concluded that the measured signals in the green (557.7 nm) and purple (391.4 nm) spectral bandpasses could not be attributed to regular atmospheric scattering effects, even though the model also showed a relation of the degree of polarization with aerosol loading.

Bosse et al. (2022b) sought to explain the polarization signals due to the average direction of motion of the precipitating electrons. They found a small correlation between the angle of linear polarization and the magnetometer data. However, the auroral signal was weak, and there were large discrepancies between the two instruments at multiple times. Laboratory experiments by Bourgeois et al. (2022) also provided a verification of the polarization of the blue line (427.8 nm) and the purple line (391.4 nm) coming from N_2^+ of the order of 3% and 5%, comparable to what was found in the aurora measurements. However, it must be noted that these measurements were done with the same polarimeter as the field measurements, so any internal systematic errors also impacted the laboratory measurements.

All previously described measurements were conducted with instruments only capable of single-point measurements that disregarded any spatial information. Since the aurora is an extremely extended phenomenon, measuring the linear polarization with an imaging camera should give more insight into the phenomena and add fidelity to the measurements, readily comparing parts of the sky with and without an aurora. Dekemper et al. (2019) and Vanhamel et al. (2021) proposed a spectropolarimetric concept amenable to imaging based on a dual-channel AOTF (acousto-optic tunable filter), with no published auroral observations to date.

Here, we introduce a novel, compact implementation of a multi-band polarimetric imaging concept specifically tailored to simultaneously measure the linear polarization signals in the red, green, and blue auroral lines. The main goals for the development of this instrument concept were:

- Imagine a wide enough field of view for auroral signals ($\gtrsim 5 \times 5$ square degrees) to detect their spatial structures and to distinguish between auroral and atmospheric scattering polarization signals.
- Instantaneous measurements of the main auroral spectral lines located in the red, green, and blue to enable simultaneous diagnostics and mutual polarization corrections.

- As the aurora is commonly a highly dynamic phenomenon, we aim to provide a high temporal resolution (<10 s) and snapshot polarimetric imaging.
- As the polarization signals in all three major spectral lines are expected to be relatively small (<10%), very small ($\lesssim$1%), or even consistent with zero, we require a challenging sub-percent polarimetric performance in terms of sensitivity (noise level in the fractional linear polarization) and absolute accuracy (level of control of instrument systematics).

Imaging of linear polarization signals can be achieved in different ways. The most frequently used approaches are temporal and/or spatial modulation of the different polarization states using polarizing optical elements to either filter different polarization states sequentially or divide them to produce separate detector images. However, due to recent advances in the field, spatial modulation can now be performed on an interleaved per-pixel level in a so-called "polarization camera" (Maruyama et al., 2018; Stockmans et al., 2024). Our instrument goals are simultaneously enabled by this novel imaging detector that features both pixelated polarization filters and RGB color filters that can be used to uniquely identify the light from the red, green, and blue passbands. These imaging devices consist of a micro-polarizer array (MPA) in front of a detector; the MPA is a layer of linear polarizers oriented in a repeated pattern matching the pixels. The combination with color filters makes the detector also color-sensitive to Red, Green, and Blue. These RGB color filters are laid on top of pixels in the common Bayer pattern, see Figure 1. After a thorough calibration, these instruments are capable of sub-percent accuracy linear polarization measurements as shown in Stockmans et al. (2024).

In this paper, we describe PANIC (Polarization of the Aurora in the North Imaging Camera), the prototype of a new imaging instrument to measure the linear polarization signal of the aurora. It is based on a combination of the MPA detectors, several additional filters, and a rotatable half-wave plate (HWP). The RGB color separation of the polarization camera matches the most prominent lines of the aurora, enabling a separation of the three main spectral signals. The addition of the HWP enables temporal modulation in addition to the spatial modulation inherent to the MPA detector, thereby enhancing the polarimetric performance.

In the following sections, we will first introduce the instrument concept and its optical layout. We motivate the choice of the filters and discuss the demodulation algorithms to derive the Stokes parameters from the raw images. In Section 5 we present the first data recorded of the aurora borealis during a field campaign in Norway and (the upper limit of) the linear polarization signal we retrieved. In the discussion section, we discuss current shortcomings and list potential upgrades of the instrument. We conclude with a summary of our findings and the current capabilities of the instrument.

2 Instrument concept

Polarization is the fundamental property of light describing the (average) direction of the electric field of electromagnetic waves upon propagation that, in the optical regime, we detect as a beam of photons. In this paper, we use the applicable description of partial polarization as described in Snik et al. (2014) using the Stokes parameters. These are defined as $[S_0\ S_1\ S_2\ S_3]^T$ or $[I\ Q\ U\ V]^T$, where we will primarily use the latter notation. The first Stokes parameter, I, is the total intensity, regardless of polarization. Q denotes the difference between the measured intensities filtered for vertical and horizontal linear polarization. A positive signal in Q implies preferentially vertically polarized light, and a negative signal in Q describes preferentially horizontally polarized light. Likewise, Stokes U describes linearly polarized light but is evaluated at $\pm 45°$. Stokes V provides a measure of the preferential rotation direction for circularly polarized light, which is not of interest in this paper. Throughout our measurements, we define $+Q$ to be parallel to the horizon and $-Q$ perpendicular to the horizon. $+U$ is then oriented 45 degrees counterclockwise from the horizon looking from the instrument.

To go from Stokes parameters to Degree of Linear Polarization (DoLP) and Angle of Linear Polarization (AoLP), we can simply combine the first three Stokes parameters:

$$\mathrm{DoLP} = \frac{\sqrt{Q^2 + U^2}}{I} \tag{1}$$

$$\mathrm{AoLP} = \frac{1}{2}\mathtt{atan2}\left(\frac{U}{Q}\right) \tag{2}$$

In this paper we will mainly focus on the fractional linear Stokes parameters, $Q/I \equiv q$ and $U/I \equiv u$, due to the ease of comparison between measurements of different intensity and descriptive systematics like (normalized) zero-point offsets. If the Gaussian noise variance of the measurement is high, this will bias any DoLP determination and skew its statistics, but the fractional linear Stokes parameters will have an unchanged mean, making interpretation easier.

Measuring polarization signals in the optical regime is challenging due to the insensitivity of typically used photodetectors to polarization. This means that some kind of modulation of the light is required, which can be done temporally, spatially, or both (Tyo et al., 2006; Snik & Keller, 2013). These different forms of polarization modulation face their specific challenges given the properties of the source. For the aurora, the source is highly dynamic, both in terms of temporal variations, as well as spatial structure. The corresponding systematics for the different concepts become apparent:

- Measurement concepts based solely on a rotating polarizer or a rotating HWP in combination with a polarizer are highly susceptible to the intrinsic temporal variation of the source, which readily induces spurious signals at the 1% level.

- Measurement concepts based solely on beam-splitters or separate boresighted systems with polarization filtering are highly susceptible to any difference between the (split) beams that are recorded separately: transmission, spatial sampling, and optical aberrations, which may also depend on temperature. Such effects also induce systematics at the ~1% level.
- A combination of spatial and temporal modulation ("dual-beam exchange") can be used to mitigate all these systematics as in Donati et al. (1990); Tinbergen (2005); Bagnulo et al. (2009), but often yields complex instrument designs.
- Single-point measurements provide very limited information on how to disentangle auroral signals from atmospheric scattering polarization. Therefore, (snapshot and multi-line) imaging is preferred, however, challenging to implement.

We propose an instrument concept that mitigates all of these limitations. It is based on a CMOS detector with a micro-polarizer array (MPA) directly attached to the pixels. This detector enables both polarimetric imaging with spatial modulation and multi-bandpass imaging due to the spatial separation of the RGB pixels. Figure 1 provides a rendering of the layout of the filters on the focal plane array by Maruyama et al. (2018). This focal plane array separates the detector into distinct pixels with sensitivity to different polarization angles and colors. By inserting a rotating half-wave plate (HWP), we introduce an additional temporal modulation to the system, which allows us to interchange the polarization filtering (cf. the dual-beam exchange) of the different pixels. The additional HWP does, in principle, not affect the snapshot capabilities of the instrument, as for every HWP position, the complete set of fractional linear Stokes parameters can be obtained. The combination of spatial modulation and temporal modulation lends itself to optimal demodulation strategies in the Fourier domain (Vaughn et al., 2015). However, jointly analyzing a full set of HWP positions (at least 4 for a full exchange of all the pixels) reduces the effective temporal resolution.

The benefit of using this system is that there is a single optical path and all intensity artifacts that can result from different lenses, filters, and optical aberrations on larger scales than a single super pixel affect all polarization channels in the same manner. Any defects or large temperature differences between different detectors are eliminated by using only one detector. Finally, the instrument is much more compact due to the use of only a single, small detector.

Nevertheless, the snapshot polarimetry and multi-line imaging with the off-the-shelf polarization camera have their own technical limitations. The detector itself is prone to noise artifacts, mostly pixel-to-pixel gain differences, and high dark currents. These artifacts translate into instrumental polarization and scaling of the real polarimetric signal as described in Stockmans et al. (2024). Next to these instrumental effects, the main artifacts come from the post-processing steps to a complete

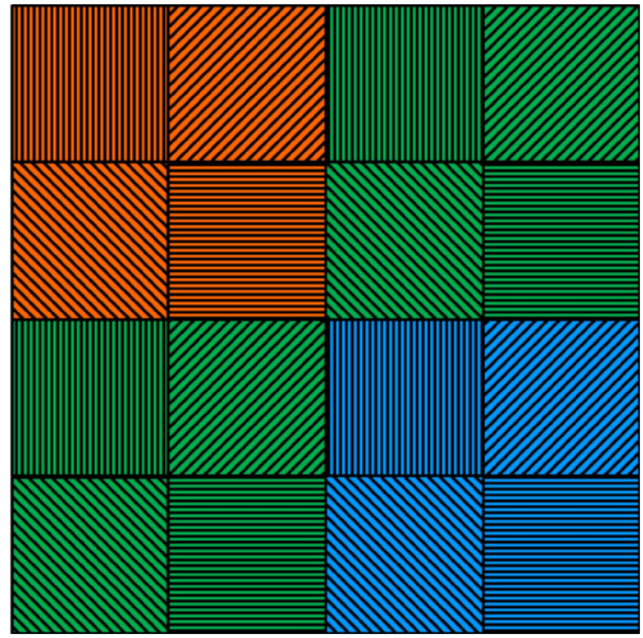

Figure 1. Layout of the filters in a 4 × 4 part of the focal plane array, known as a "superpixel". We see the Bayer RGB pattern overlaid with the wiregrid polarizers at four angles. Image copied from Figure 14b in Maruyama et al. (2018).

image. These errors are called "instantaneous field of view" (IFOV) errors, and were first described in Ratliff et al. (2006). Each pixel samples its own small part of the field of view (FoV) and has its own sensitivity to a specific polarimetric orientation and color. The smallest set of pixels that contains all variations of linear polarization and RGB filters is called a "superpixel". It consists of 4 × 4 = 16 detector pixels, that all sample a slightly different part of the source. This mismatch in spatial sampling can lead to the creation of false signals in the reconstructed multi-bandpass polarization image. The post-processing steps to create a complete image in all channels are called "demosaicing". Demosaicing is the combination of the intensity data of the different pixels given the known layout of the filters to retrieve the separate linear Stokes and color images. The IFOV errors are caused by simple intensity gradients being translated into a false polarimetric signal or a wrong color signature. The sharper these gradients are, the stronger the false signal will be. In this paper we use two main methods of demosaicing: "superpixel"-based (Tyo et al., 2009) and Fourier-based (Hagen et al., 2024). The former is simpler to implement, but the latter is less prone to these IFOV errors. For aurorae, we expect distinct narrow arcs or curtains to cause more IFOV error due to their strong intensity gradients. On the other hand, we expect broad, diffuse aurora to be less prone to this problem. However, stars being bright point sources have the largest possible intensity gradient over their PSF and are consequently extremely affected by these errors.

There is one final complication of using an RGB-based detector, which is the broad spectral sensitivity of the pixels. To obtain the best measurements, all contaminating light at other wavelengths than the aurora lines needs to be filtered out. It is possible to add one or multiple spectral filters, which, when combined, only have transmission peaks at the desired wavelength ranges. The filter stack can be a combination of multi-bandpass filters (Jiang et al., 2023), notch filters, or cut-off filters. Using these filters, the light in the relevant spectral bands at the aurora emission bands can be carved out, while unwanted light is either reflected or absorbed, see Figure 6 for the practical implementation.

3 Polarimetric implementation and calibration

To derive the linear polarization images for the three different color channels from the reduced images, we use two rather different demosaicing algorithms. The simplest demosaicing algorithm is "super-pixel" demosaicing, used for instance in Ratliff et al. (2009). Given the original filter layout on the detector as displayed in Figure 1, it simply estimates the separate Stokes images as:

$$I_{i,j} = \frac{1}{4}\sum_{a=0}^{1}\sum_{b=0}^{1} I'_{2i+a,2j+b}\,, \quad (3)$$

$$Q_{i,j} = \frac{1}{2}[I'_{2i,2j} - I'_{2i+1,2j+1}]\,, \quad (4)$$

$$U_{i,j} = \frac{1}{2}[I'_{2i+1,2j} - I'_{2i,2j+1}]\,, \quad (5)$$

where the left-hand side are the respective Stokes images, i and j are the indices of the super-pixel, and I' is the mosaiced image corrected for the dark current, bias, and flat field. The indices will switch according to the layout of the effective polarizer angles.

The other approach, based on the Fourier-demosaicing method, requires more intermediate steps. First, the discrete Fourier transform of the mosaiced image is taken. Due to the periodic mosaicing pattern, the Fourier image is divided into different components related to the different color and polarization channels. From the 2D Fourier transformed image, the nine components (three colors times three Stokes parameters) are spatially filtered and combined according to precalculated ratios to retrieve the Fourier transforms of the separate linear Stokes for all the separate color channels. From these distinct arrays, all separated linear Stokes images for all three color channels are retrieved through an inverse discrete Fourier transform (Hagen et al., 2024).

To enhance the polarimetric performance of our measurements, we implement a beam-exchange approach, which is common in astronomical polarimetry, by using a rotating HWP. Rotating a HWP in steps of 22.5 degrees in front of the detector implies that the orientation of the polarimetric channels rotates through the 0, 45, 90, and 135-degree linear polarization orientations. Whenever the fast axis of the HWP is perpendicular or parallel to the original orientation of the wire-grid on the filter, the polarization orientation of a pixel remains unaffected. However, when that angle is 22.5 degrees, the pixels that were sensitive to $I+Q$ and $I-Q$, respectively, will become sensitive to Stokes $I+U$ and $I-U$ instead, and vice versa. An angle of 45 degrees means that the pixels originally sensitive to Stokes $I+Q$ or $I+U$ will become sensitive to Stokes $I-Q$ and $I-U$, respectively, and vice versa.

To still be able to use equation (3) for calculating the linear Stokes parameters, the indices are changed according to the changing effective linear polarizer direction. For the Fourier-demosaicing algorithm, the spatially filtered components are interchanged and should be switched back to their original location before being combined with the separate Stokes channels.

The two main detector systematics that cause artifacts in the data are pixel-to-pixel signal variations for constant intensity and a high dark offset. The signal variations can be due to a difference in pixel filter transmission efficiency, a variation in the gain of the pixel, or varying instrumental transmission effects such as vignetting. The dark offset is primarily due to the thermal excitation of the electrons (dark current), which are indistinguishable from photon-excited electrons, and a low electronic bias. We have based our reduction on Stockmans et al. (2024), but slightly simplified our reduction steps by only focusing on a single exposure time and gain to speed up the process. Eventually, the instrumental artifacts are removed by flat-fielding the instrument and subtracting the estimated dark offset. As a mathematical formula:

$$I' = \frac{I_{\text{raw}} - D}{F - D}, \quad (6)$$

where I' is the corrected intensity frame, I_{raw} is the raw intensity frame, D is the estimated frame of the dark offset, and F is the flat field taken at the same wave plate angle.

The dark offset of the detector depends strongly on the temperature. Since the temperatures are likely to vary strongly during (outdoors) measurements during winter nights at high-latitude locations, obtaining a good estimate of the dark offset poses the biggest challenge in this work. Any overestimation of the dark offset leads to an increase of the measured fractional polarization signal relative to its actual value due to an underestimation of I, while not affecting Q and U. Underestimation of the dark offset, on the other hand, decreases the retrieved fractional polarimetric signal compared to the original polarimetric signal, this time by overestimating I. To give an example, a weak signal measured by our detector with an intensity I of 5 counts and an overestimation of the dark offset by 1 count causes a real polarization signal of 0.01 in q to be measured as a polarization signal of 0.0126. This is a relative overestimation of 25%.

Pixel-to-pixel signal variations, on the other hand, have a larger influence on the absolute polarimetric accuracy but are easier to correct for. These pixel-to-pixel variations induce a signal difference between the different channels, which will shift the polarimetric zero-point of q and u away from zero. This means that an unpolarized source will suddenly show a polarimetric signature, which is purely reflecting the differential gain or transmission variations.

To calibrate these pixel-to-pixel signal differences, we obtained flat-fields using a six-inch (15.24 cm) integrating sphere (Edmund Optics part #58-586) placed at one meter distance. The full FoV of the instrument was within the exit port of the integrating sphere, in principle providing an uniform illumination of the FoV of the instrument. Any measured brightness differences were in turn caused by the pixel-to-pixel gain differences and transmission artifacts such as vignetting.

However, there is one rotating element in the optical train, which changes the pixel-to-pixel illumination artifacts according to its rotation. To see the effect of the HWP on the pixel-to-pixel variations, we rotated the HWP in four steps of 22.5 degrees and took images of the integrating sphere at each orientation. The four flats were averaged, resulting in the mean flat as seen in Figure 2. In Figure 3, we show the relative difference between the mean flat compared with each of the four flats at a different angle of the HWP to show the stability during its rotation. Here we see an optical ghost rotating through the FoV and higher differences at the edges than in the center of the FoV. To remove the effects of the ghost and the deviation at the edges of the image, we crop all the results to within the most stable part marked in red. The stability of the flats within the red rectangle while rotating the HWP is considerably less than a percent; any residual systematic errors due to the pixel-to-pixel variations are therefore expected to be sub-percent as well.

To remove the residual systematic instrumental effects of the pixel-to-pixel gain and illumination differences, we use the beam-exchange approach and combine the measurements using the double difference as described in Tinbergen (2005); Bagnulo et al. (2009); Snik & Keller (2013). The double difference uses the beam-exchange method to flip the sign of the sensitivity of the measurements and then averages over them:

$$\frac{\hat{Q}}{\hat{I}} = \frac{1}{4}\left[\frac{(I+Q)_1-(I-Q)_1}{(I+Q)_1+(I-Q)_1} - \frac{(I-Q)_2-(I+Q)_2}{(I-Q)_2+(I+Q)_2}\right], \quad (7)$$

$$\frac{\hat{U}}{\hat{I}} = \frac{1}{4}\left[\frac{(I+U)_1-(I-U)_1}{(I+U)_1+(I-U)_1} - \frac{(I-U)_2-(I+U)_2}{(I-U)_2+(I+U)_2}\right]. \quad (8)$$

Since we take multiple frames in between rotating the HWP, we first averaged over the N frames with the same HWP orientation. Furthermore, we only combine the measurements that differ in a HWP angle of 45 degrees since those have switched the polarization orientation between the same pixels. This method minimizes the inherent systematics of the detector. Every residual, static detector defect that leads to a false polarization signal is inverted for the second measurement and, to first order, averages out. The following formula shows the implementation for the fractional q, the implementation for u is the same.

$$q_{dd} = 0.5 * (\frac{q_1 + ... + q_N}{N} - -\frac{q_{2N+1} + ... + q_{3N}}{N}), \quad (9)$$

where q_{dd} is the fractional Stokes parameter as calculated with the double difference, q_i is the fractional Stokes parameter q at frame i calculated by equation (3) after reduction by equation (6). Finally, N is the number of measurements taken between changing the angle of the HWP.

4 Instrument prototype and field campaign set-up

The instrument concept was developed into a prototype to proof its principle. The optical train of PANIC contains six optical parts, which are:

- A 1-inch half-wave-plate, achromatic between 400–800 nm (Thorlabs AHWP10M-600), mounted in a motorized rotational stage (Thorlabs KPRM1E/M).
- A notch filter by Chroma blocking a small band around 473 nm (ZET473NF). Placed in a removable mount.
- A triple bandpass filter by Chroma peaking in transmission around 405, 488, and 594 nm (ZET405/488/594). Placed in a removable mount.
- A shortpass filter with a cut-off filter at 650 nm and with a blocking capability of OD4 by Edmund Optics (#84-712). Placed in a removable mount.
- A 1-inch machine vision lens with a 50 mm focal length by Thorlabs (MVL50M23).
- Finally, the color-polarization camera by LUCID Vision Labs (TRI050S1-QC) with MPA IMX264MYR chip by Sony.

These optical components were housed in a 3D-printed case, specifically designed to be as compact as possible to maximize mobility and ease of use. The housing was printed using an Original Prusa i3 MK3 printer with a black Polyterra PLA filament with a 15% plastic fill factor. This low fill factor means that the housing was mostly hollow, enhancing its thermal insulation properties. The detector and HWP rotation stage were directly attached to the housing. The lens was attached with a C-mount to the detector. Finally, the filters were placed in movable filter mounts. The filter mounts were designed to be able to slide in and out of the optical path and be held in place using small magnets on either side. Figure 4 is a schematic of the layout of the optical elements. Figure 5 shows the technical drawing of the instrument.

Due to the compact size ($25 \times 22 \times 10.5\,\text{cm}^3$) and the light weight (~0.8 kg) of the instrument, it can be easily handled and carried by a single person. To conduct the measurements, we mounted the instrument on

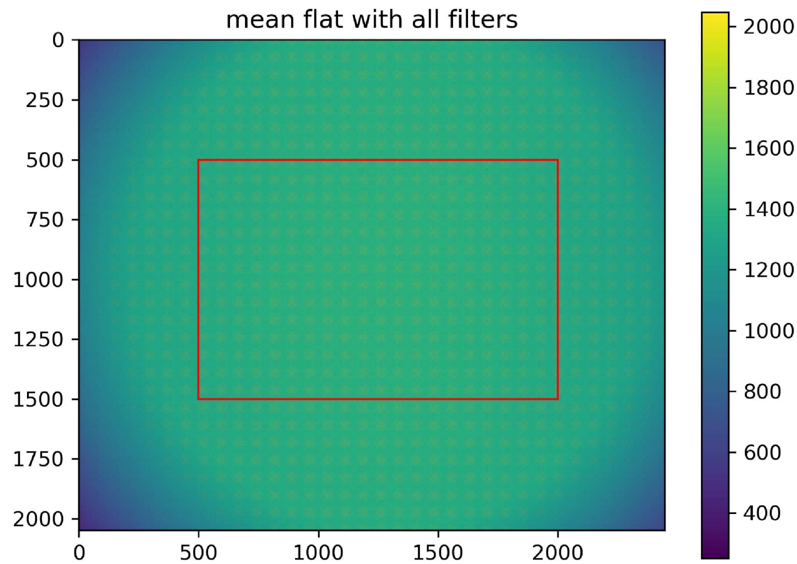

Figure 2. Mean flat made by looking directly into the entrance port of an integrating sphere, ensuring uniform and unpolarized illumination. The red rectangle depicts the region of interest (ROI) used throughout this paper.

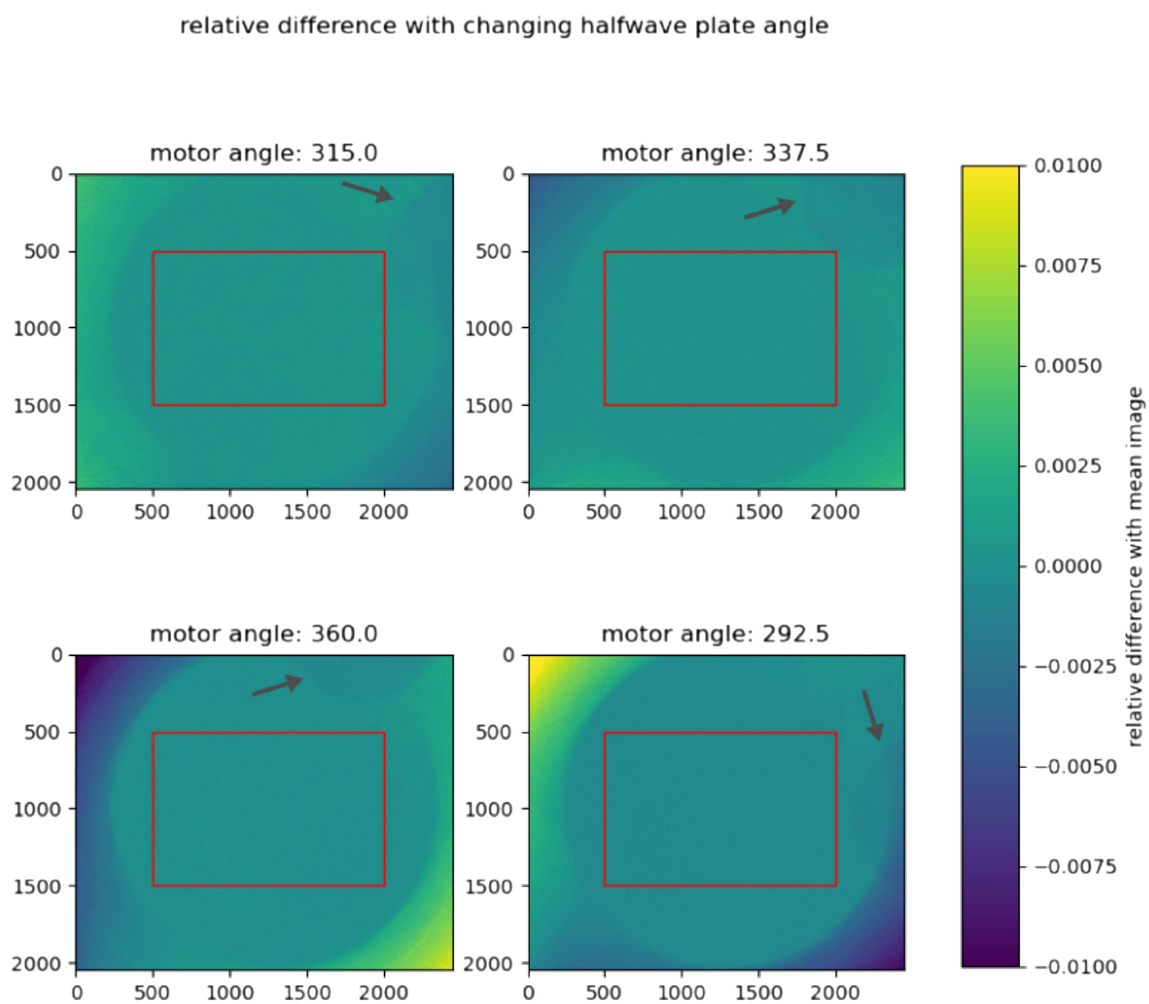

Figure 3. The fractional deviation of the flats at different HWP positions obtained with a uniform, unpolarized illumination by an integrating sphere. When the angle of the HWP is changed, it moves the position of a ghost, as indicated by the gray arrows. The red rectangle depicts the region of interest.

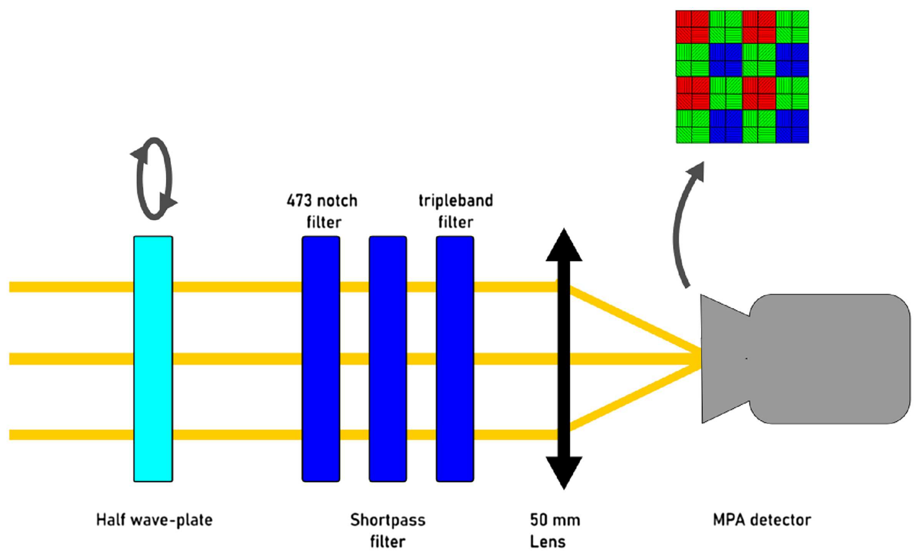

Figure 4. Schematic of the optical elements of the PANIC instrument.

a commonly available photography tripod using a standard mounting plate attached to the bottom of the instrument. There were two cables running from the instrument to control the detector and the rotating motor of the HWP. All control software was written in Python and ran directly on a laptop connected through these cables. The control code made use of the software from LUCID Vision Labs, Inc., for the detector. For the rotating motor, we made use of the software provided by the KINESIS software by Thorlabs, Inc., combined with the public pyLabLib module by Shkarin (2022). Additionally, we mounted a temperature sensor inside the casing to be able to record the temperature inside the housing.

The detector itself has 2048 × 2448 pixels, which in combination with the focal length of the lens, meant that the instrument's FoV was 8.083 × 9.655 degrees. The spatial resolution of each individual pixel was 14 × 14 arcseconds squared. The data was digitized by a 12-bit ADC. The detector supports a 0–24 dB gain increase and a 24–48 dB digital gain increase. Furthermore, the exposure time could be set manually to a maximum of 10 s.

The listed spectral filters were chosen to reduce the instrument's sensitivity to all wavelength regimes apart from the lines of interest while trying to minimize the total number of filters. We expect the main contamination signal to be due to background broadband sources, such as street lights of the neighboring town and stars. In Figure 6, we show the estimated quantum efficiency and total system throughput per wavelength band for the three differently colored pixels. In the future, the total system throughput per wavelength can be measured in the lab with the use of a monochromator and a radiometer. Alternatively, the calibration can be done as in Burggraaff et al. (2019) using an add-on with a slit and a grating to record a spectrum of a light source with a known spectrum (e.g., the spectrum of the Sun) onto the detector.

As can be seen in Figure 6, there is still a crosstalk in spectral sensitivity where the blue channel is still sensitive to the green aurora, the green channel to the red, etc. This cannot be solved with uniform filters since all channels would be affected equally. However, given a correct dark offset subtraction and the absence of any parasitic light besides the aurora, we can calculate the original intensities for the three channels. It is possible to construct a filter crosstalk matrix $\mathbf{M}$ given the total system throughput of the three channels. To correct for the spectral crosstalk, we multiply by the inverse, $\mathbf{M}^{-1}$, with the measured intensities $\mathbf{I}$ to retrieve a vector of the auroral signals $\mathbf{S}$:

$$\mathbf{M} = \begin{pmatrix} R(427\,\mathrm{nm}) & R(557\,\mathrm{nm}) & R(630\,\mathrm{nm}) \\ G(427\,\mathrm{nm}) & G(557\,\mathrm{nm}) & G(630\,\mathrm{nm}) \\ B(427\,\mathrm{nm}) & B(557\,\mathrm{nm}) & B(630\,\mathrm{nm}) \end{pmatrix}, \tag{10}$$

where each component is the total system throughput of that color channel evaluated at the specified wavelength.

$$\hat{\mathbf{S}} = \mathbf{M}^{-1}\vec{\mathbf{I}} \tag{11}$$

To validate the full instrument, we conducted a field campaign at the Skibotn observatory in Norway at N 69°20′53.233″ E 20°21′47.993″ from 5 February 2024 until 13 February 2024. During this period, multiple nights were overcast, and some other nights with clear skies saw little to no auroral activity in the accessible part of the sky. There was, however, one night during which the conditions were more favorable, and we show the results of those observations below.

The observations were taken pointing towards the north and north-north-east at an approximate declination between 30 and 60 degrees. The nearby village of Skibotn is located northwest of the observatory at a distance of about 6 km.

Although the instrument had a protective, insulating layer due to the 3D-printed housing, the extreme outside

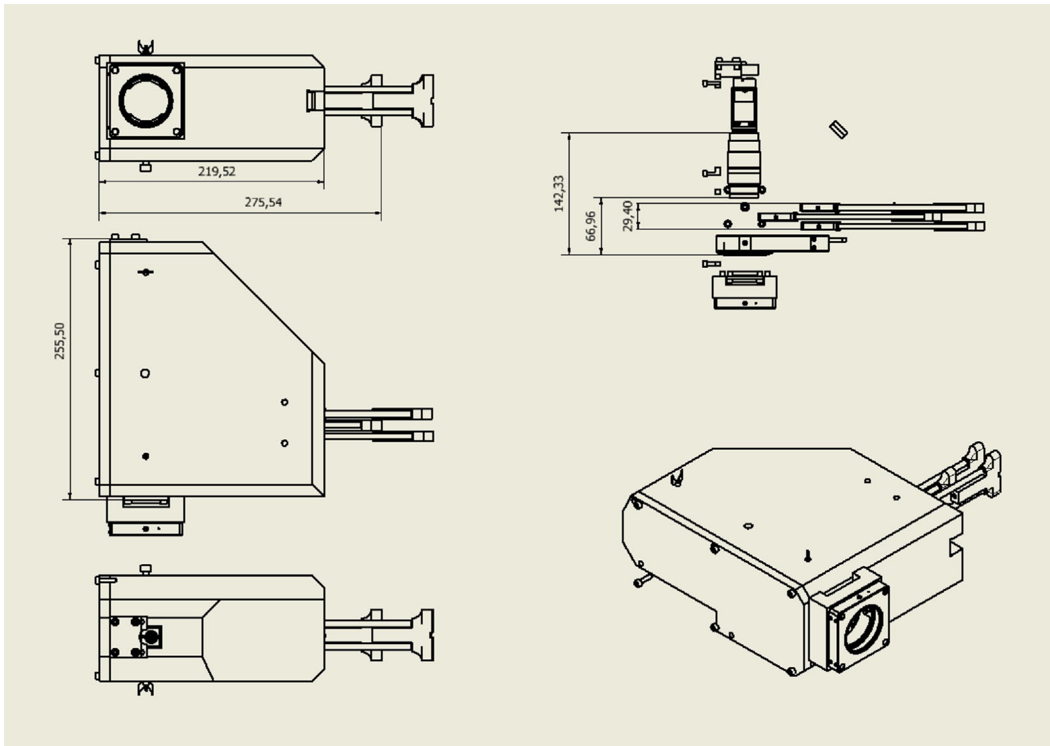

Figure 5. Technical drawing of the PANIC instrument with its 3D-printed case. Measurements are given in mm.

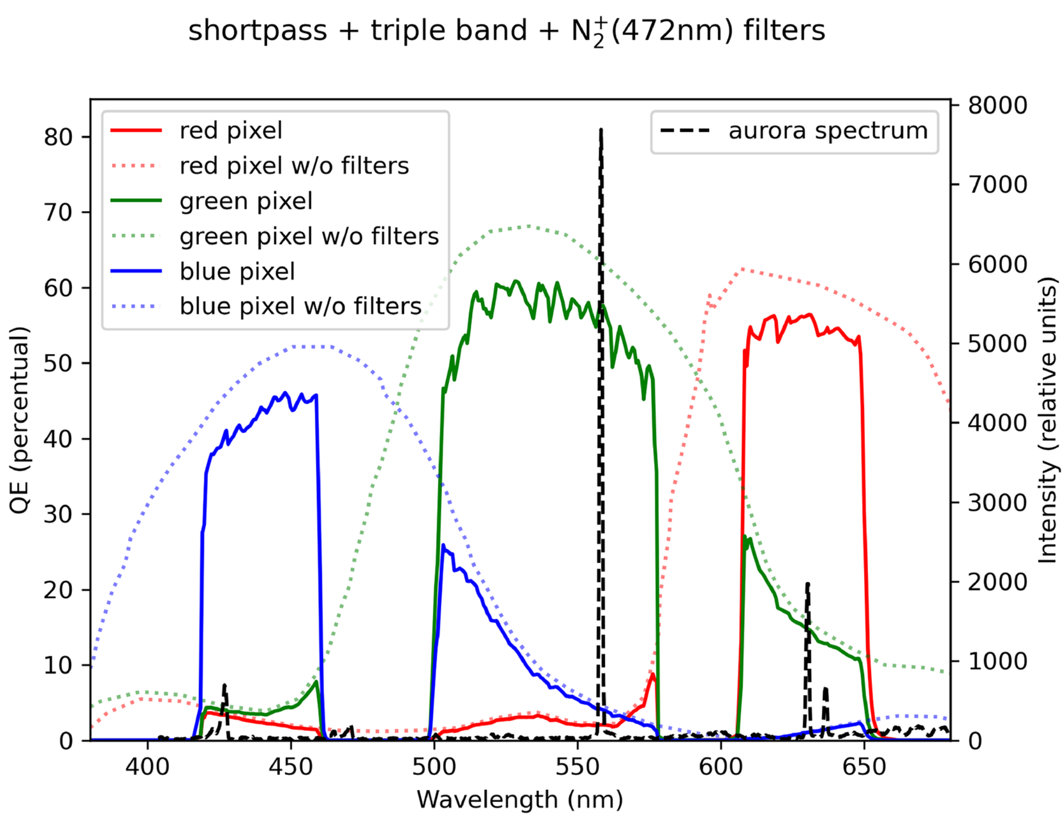

Figure 6. The quantum efficiency as a function of wavelength of the three different pixels and total system throughput after the spectral filters. This is an estimation based on manufacturer data (LUCID Vision Labs, 2018). Overlaid is a spectrum from an aurora showing the relative intensity as a function of wavelength.

temperatures were a complicating factor. The temperature varied throughout the measurement period between −15 and −23 °C, with constantly changing wind conditions. The internal temperature of the instrument varied even more wildly, depending on the time the instrument had been running, the time the instrument had been outside, and whether the wind was directed at the viewing port.

Due to complications with the rotating motor, we were forced to put a heating element close to the instrument, which caused additional variations in the internal temperature. The detector temperature was usually between 27 and 51 °C. We show a more in-depth view of the changing temperatures of the detector and the related dark offset of the instrument in Appendix B.

Although the detector has a temperature sensor that saves the temperature of the device during measurements, this sensor has two main shortcomings: the temperatures are saved with 1-degree Celsius accuracy, and the temperature of the detector is not necessarily the temperature of the whole sensor chip. Especially during some high-temperature gradients, the chip and other parts of the detector are not necessarily in thermal equilibrium. These two shortcomings complicated a correct estimation of the dark offset.

Finally, the observations were done by taking frames of 10-second exposure time using an instrument gain of 24 dB. The HWP was rotated every five frames by an angle of 22.5 degrees. The rotation was done with a cycle of 16 steps anti-clockwise followed by 16 steps clockwise, since the rotation angle might drift after too many steps in one direction.

5 Prototype results

In this section, we present the data of the night from 11 to 12 February 2024, which contained the highest auroral activity during the field campaign. To give a measure of how strong the activity was and when it peaked, we show in Figure 7 the keogram over the night from the nearby all-sky camera (Nanjo et al., 2022). The keogram shows clear bursts of auroral activity from 21:45 onward.

First, we needed to correct the measurements using the flat field and estimated dark offset frame for each measurement. While actions were taken to try to stabilize the temperature of the instrument, this was not fully successful, and the temperature varied by more than 30 degrees between measurements. The internal temperature variation is shown in more detail in Appendix B. We had access to dark offset frames at multiple temperatures taken using the same settings but with a lens cap to block the light from entering the instrument. These dark offset frames showed a spatial non-uniformity, showing the importance of removing the whole frame instead of only the median dark value. Sub-Kelvin temperature differences between the measured dark frame and the measurement meant that the dark offset could differ by multiple counts.

To still get the most accurate dark offset subtraction, we scaled the available dark frames. Using the detector temperature during a measurement, the available dark frame with the closest matching temperature was selected. The scaling factor was then determined by estimating the median dark offset from the data itself and scaling the median of the available dark frame to match the median of the estimated dark offset.

To estimate the median dark offset of the measurements, we assumed that only the green aurora is present in the data and that all other signal is due to the dark offset. The median dark offset is the same for all three color channels, since it is inherent to the CMOS detector. Given the approximation and the parameters from equation (10), the mean raw intensity of the different color channels is then:

$$I_b = d + B(557\,\text{nm}) * S_{557}, \tag{12}$$

$$I_g = d + G(557\,\text{nm}) * S_{557}, \tag{13}$$

$$I_r = d + R(557\,\text{nm}) * S_{557}, \tag{14}$$

where $I_{b/g/r}$ is the raw median intensity for the blue, green, and resp. red channel, d is the median dark offset, and S_{557} is the signal of the green aurora.

To estimate the median dark offset with the approximated sole presence of green aurora at 557 nm, the mean dark offset can be estimated as the minimum value of either the green aurora-corrected blue, red, or green channel median intensities:

$$d_{\text{est}} = \min\left[\frac{I_b - r_b * I_g}{1 - r_b}, \frac{I_r - r_r * I_g}{1 - r_r}, I_g\right], \tag{15}$$

where $r_b = \frac{B(557\,\text{nm})}{G(557\,\text{nm})}$ and $r_r = \frac{R(557\,\text{nm})}{G(557\,\text{nm})}$. The approximation neglects any other aurora signal or parasitic light and is therefore only used in the estimation of the dark offset and not in the other post-processing steps. Any auroral signal around 630 nm or 427 nm would cause a slight over-subtraction of the dark, which would result in a lower reported intensity of all three lines and a slight overestimation of the fractional polarization signal. The overestimation of the fractional polarization scales with the actual strength of the polarization signal. In practice, using this method of estimating the dark offset will result in the faintest of the three color channels being set to approximately zero. This adjustment greatly increases the impact of noise on the fractional Stokes parameters measured for that channel. Since the blue intensity is almost always the faintest of the three, it will render the blue channel highly unreliable.

The main parasitic light source in the data is stars. Since the brightest stars are easily identifiable, they are removed before the estimation and any polarimetric calculation. The stars are identified in the image by running DAO starfinder (Stetson, 1987) as implemented in Astropy by Astropy Collaboration et al. (2022). The removal of those stars from the raw frames is done by setting a square of ten by ten pixels at the approximated location of the star to zero intensity and polarization.

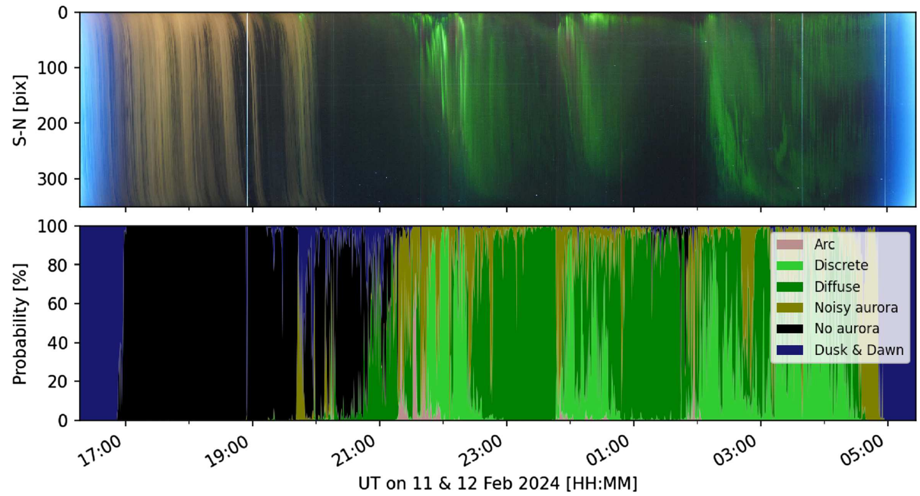

Figure 7. Keogram of the ASC01 camera from the Norwegian Observatory of Space Weather (NOSWE) in Skibotn, Norway. It displays a sliced view from an all-sky camera during the night. PANIC is directed at around S-N (South-North) 100. The green bursts after 21:45 indicate auroral activity, while the brown patches at the beginning of the night indicate clouds. Retrieved from https://tromsoe-ai.cei.uec.ac.jp/#/Archive.

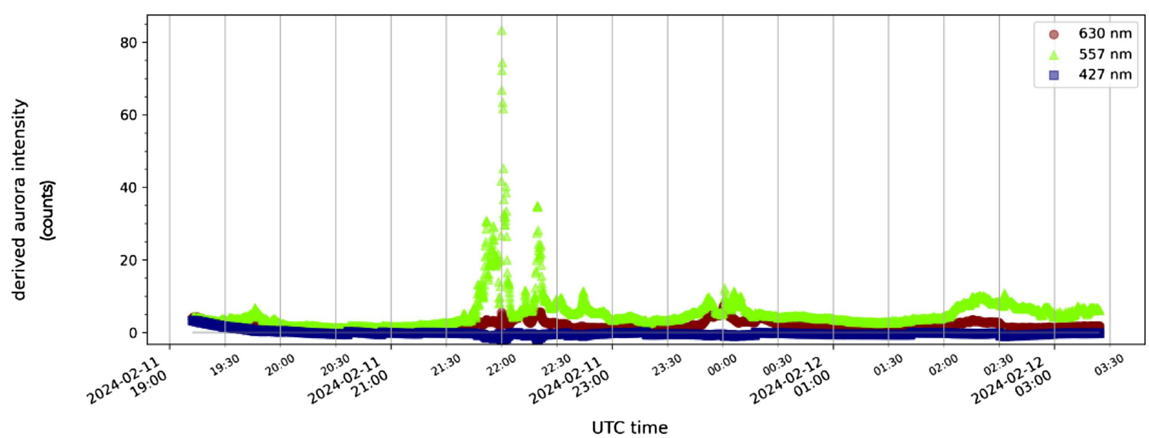

Figure 8. Estimated intensity in digital counts of the 427.8 nm line (in blue), 557.7 nm line (in green), and the 630/636/639 nm triplet (in red).

Using the estimated dark frame, the measured flat field, and equation (6), we are able to reduce the data.

5.1 Measurements of the mean properties over longer timescales

In Figure 8 is the respective mean aurora intensities calculated using the matrix multiplication described in equation (10). We see a clear signal of the green 557.7 nm aurora and the red 630 nm aurora. However, the 427.8 nm line is mostly around zero, while sometimes showing unrealistic negative intensity values. This is mostly due to the dark offset subtraction algorithm that we used, and there is a minor over-subtraction of 1–3 counts in regions of stronger red aurora.

From the reduced data, we could also determine the progression of the mean fractional Stokes parameters during the night. However, using the fractional Stokes parameters coming from the snapshot demosaicing with equation (3), the data is rather noisy. These images are displayed and discussed in Appendix A. Using a moving window of twenty images, we were able to estimate the standard deviation on the fractional polarization parameters due to changing systematics. We found a typical uncertainty of between 0.02 and 0.05 for q and u outside of auroral activity and 0.01 during auroral activity. For now, we mostly focus on the data from the double difference method. The uncertainty after using the double difference method is halved to 0.02–0.01 outside of auroral activity and 0.006 during auroral activity. The temporal resolution of the snapshot measurements is 10 s. However, for the double difference processed results, this is extended to 2 min. In Figure 9 we show the intensity during the night measured as well as q and u calculated with the double difference method.

It shows that the polarization tends to zero during bright events, while being large in periods where the aurora is absent. At the beginning of the night, we measured significant amounts of sky polarization in the absence of an auroral signal, although it has a high uncertainty. This sky polarization is evident from the fact that all three RGB channels exhibit a similar polarization signal evolution up to ∼6% along a constant angle of linear polarization (determined by the combination of q and u). This angle is roughly 22.5 degrees from the horizon.

Upon the appearance of an auroral outburst, predominantly in the green channel, the measured polarization tends towards zero. Even if we corrected for an underestimation due to excessive dark removal of up to 4 counts, this could only increase the signal by ∼10% and not be enough for a 3-σ detection. Our leading explanation is that when the auroral brightness is much higher than that of polarized scattered light in the sky, in combination with the green line polarization being small if not zero, the total measured polarization signal in the green channel is subdued. Since the intensity of the auroral outburst is a factor of ten to twenty times higher than the intensity of the parasitic light at the beginning of the night, the measured DoLP would drop to 0.006 or even 0.003 if the aurora were unpolarized. The random photon noise also relatively decreases with the acquisition of many more photons. After the first auroral outburst, the sky contribution becomes a dominant factor again. Some faint red aurora pertains, and a slightly higher polarization in the red is measured. Overall, the signals in the blue band remain erratic because of the very low intensity.

In the initial data, the Q and U switched every time the motor carrying the HWP changed direction. We believe that this was due to a 22.5-degree step of the HWP that was not tracked properly by the control code while changing direction. This effect was removed in further processing for the figures displayed in this paper.

5.2 Imaging linear polarization

The brightness of the aurora can vary from the brightness of a full moon to the brightness of the Milky Way. The measured signal-to-noise ratio is, of course, heavily correlated with the brightness as is the possibility for any imaging capabilities of the instrument.

To show the instrument's imaging capabilities, we took the measured image during the brightest peak of the night around 22:00. In Figure 10 we show the Stokes parameters for all color channels at the same scale, showing a bright signal in the green intensity. We plotted the fractional Stokes parameters in Figure 11 and see no structure in the polarization. Note that the red, green, and blue channels are not corrected using equation (10) to match the expected intensities of the auroral lines. To estimate the expected standard deviation of the fractional Stokes parameters of the image, we combined expected photon noise related to the mean I of the image and the standard deviation of the dark offset frame through a square root of the sum of squares and propagated both for the fractional Stokes parameters. The propagation was done by:

$$\sigma_q = \frac{\sigma_I}{I}\sqrt{2+q^2} \quad (16)$$

$$\sigma_u = \frac{\sigma_I}{I}\sqrt{2+u^2}\,, \quad (17)$$

where σ_I is the combined standard deviation of I from the photon noise and the dark offset uncertainty. For the red and blue channels, the latter (dark offset variation) is the dominant factor, and for the green channel, the former (photon noise) is the dominant factor. We neglected other terms such as Johnson noise and 1/f noise. The estimated standard deviation seems to match the distributions quite well.

6 Discussion

The data presented in this paper show the capabilities of our new instrument. We are able to measure the average fractional linear polarization of brighter green aurora events with a typical uncertainty of 0.006. However, this uncertainty increases to 0.03–0.05 under low-light conditions.

The instrument concept fulfills the initial requirements that we set out at the beginning of this paper. It is possible to conduct imaging polarimetry over a FoV of ∼9 squared degrees. The instrument has multi-band pass spectral sensitivity, meaning it can monitor several auroral lines simultaneously. High polarimetric accuracy is possible due to accurate calibration and the addition of an HWP. There is the option for snapshot imaging with a temporal resolution of 10 s, available for more dynamic and bright events. However, in practice, additional temporal modulation is needed, and we are limited to a lower temporal resolution of 2 min.

The field campaign also highlights some major shortcomings. The first primary obstacle is the low-light condition of anything outside of times of bright aurora. During these conditions, the noise is dominated by the variations in the dark offset, and the sensitivity becomes very low. To try to accumulate enough signal, we were forced to use the longest available exposure time and high analog gains. As a result, the true spatial capabilities of the instrument are now only accessible during very bright events.

The second main shortcoming is the temperature instability. Since the temperature of the instrument determines the amount of dark offset, all changes in the temperature lead to hard-to-model spurious signals. Furthermore, when the temperature became too low in the casing, we found that the rotation stage of the HWP stopped operating. While the freezing of the motor does not render the instrument useless, the polarimetric accuracy is reduced due to the unavailability of the double difference method used in reduction.

Future upgrades to the instrument are related to these major shortcomings:

– The first limitation of low-light conditions is difficult to mitigate. The light-gathering power of the instrument is determined by the étendue of the imaging

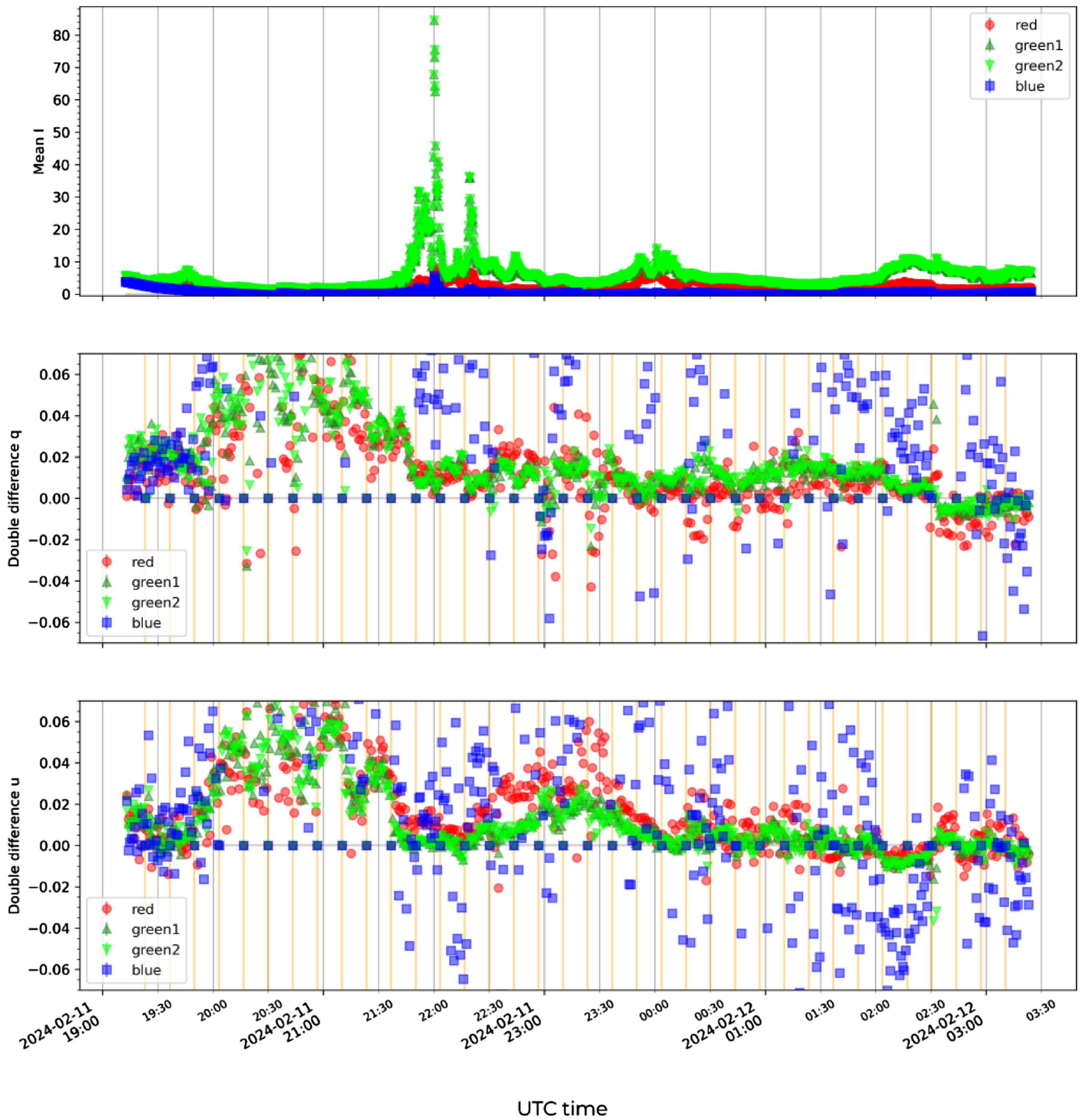

Figure 9. Overview of the night of 12 February 2024 at Skibotn, with the brightest event recorded at 22:00 UTC time. The upper figure shows the mean Stokes I in counts of the frames over time. The middle panel shows the progression of q using the double difference method against the mean time of the measurements. The lower panel shows u using the double difference method. The yellow lines indicate when the HWP changed the direction of rotation after having completed a full cycle; at these points, the double difference method returned approximately zero due to the flipping of the sign.

optics on the polarization detector: the combination of the (intermediate) pupil and the FoV emerging from that pupil. We have now used a compound lens with an F-number of 2.8, which cannot be decreased more than a factor of ~2 without inducing too many optical aberrations. A custom optical design with a larger effective pupil would collect more light and give rise to a trade-off for the FoV on the sky. Nevertheless, relatively long exposures are unavoidable, and a photon-hungry technique like polarimetric imaging remains best suited for bright events.

- Adding an internal temperature control system would reduce the huge temperature fluctuations. This increased thermal stability would simplify and optimize post-processing steps, and keep the instrument operational during measurements. It would also enable a better monitoring of the blue lines.
- Adding a custom multi-bandpass filter would single out the specific auroral lines even better and reduce contamination by spurious light sources. These sources include not only spectral lines and molecular band emission not related to the aurora, but also light from the unpolarized continuum, which dampens any relevant polarization signatures.
- Enhancement of the data-driven referencing of the zero points in q and u. If a theoretical framework

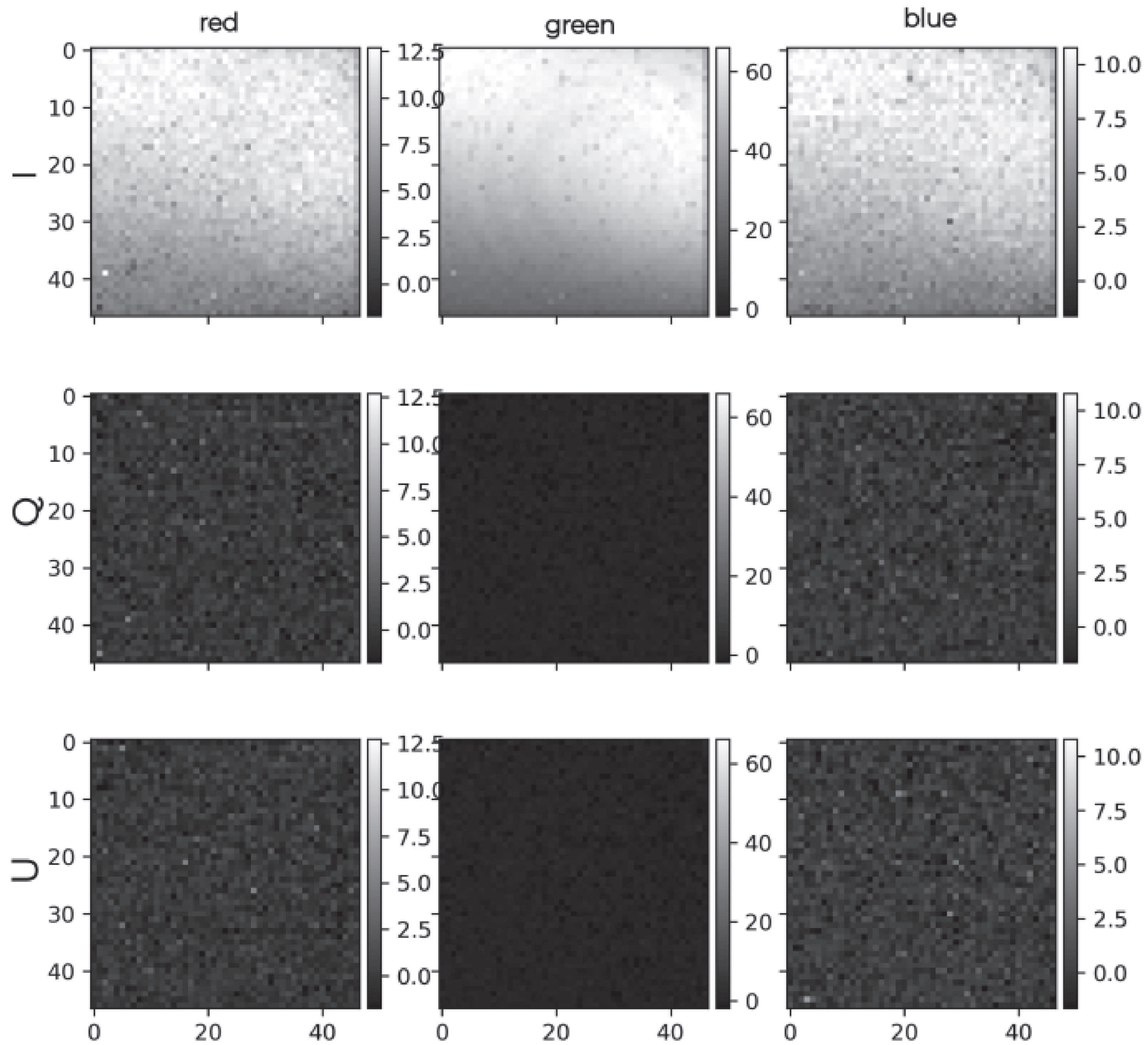

Figure 10. The pure Stokes parameters I, Q, and U for the brightest event shown on the same scale, which is dominated on the positive side by I.

concerning the expected polarization degrees of the aurora is developed, the zero points can be referenced to these known quantities. Bright stars are practically unpolarized within the sensitivity and resolution of our instrument. However, due to the sharp gradients along the PSF of the stars, demodulation is a challenge. To obtain better results, we could fit a PSF demodulation model to the stars, possibly in combination with a slight defocusing of the instrument to preserve the large-scale aurora.

– Combine the measurements with other instruments such as spectrometers, point-source monochromatic polarimeters, point-source spectro-polarimeters, and imagers.

Compared to the previous literature, we found considerably less polarization during the auroral events. To give fully conclusive rates of polarization of the aurora, it is important to reduce the uncertainties on the averaged q and u below 0.01 for fainter signals as well. The systematics of the instrument need to be understood and removed correctly so that the intrinsic noise becomes the main limiting factor.

7 Conclusion

We have introduced and prototyped a new instrument concept to spatially resolve the polarization properties of the aurora over a FoV of ∼9 degrees in diameter. We showed the data taken with a prototype called PANIC during a field campaign in northern Norway, where we observed the aurora for a week. One night, containing the brightest aurora events during the campaign, is further analyzed to show the capabilities of the instrument. For weaker events, the progression of the mean fractional Stokes parameters q and u can be monitored. We find a maximum polarization signal of $1 \pm 0.6\%$ in q during bright events using the averages of the images. During moments of no obvious aurora at the beginning of the night, we find higher polarization signals of up to 6 $\pm$

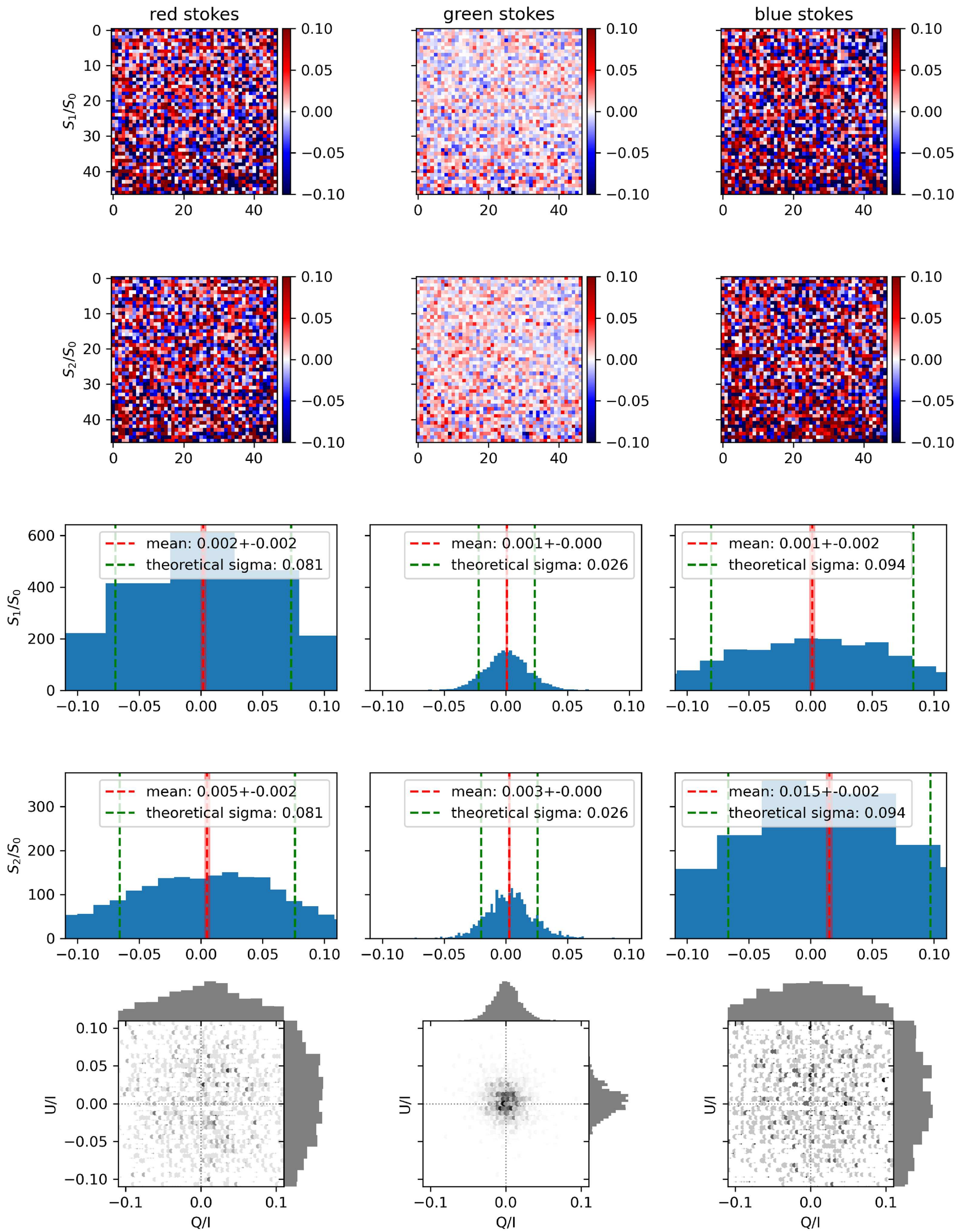

Figure 11. q and u for the brightest event in the sequence. The upper three panels show q for the red, green, and blue channels, respectively. The second three panels show the corresponding u. The third three panels show a histogram of q in the red, green, and blue channels where we show the average of the histogram with a red line and the estimated standard deviations in green. The fourth panel shows the same but for u. The final three panels show the density plot of q on the x-axis and u on the y-axis and the collapsed histogram matching the histograms in the third and fourth panels.

3%. These signals are correlated with clouds, which reflect light from a neighboring town.

We show that the instrument is capable of spatially resolving aurora in intensity. However, spatially resolving the polarimetric quantities is only possible for very bright events.

Future upgrades are proposed to reduce the main shortcomings of the instrument prototype such as low sensitivity and thermal stability. These upgrades include optimization of the throughput and the FoV, internal heating elements, custom spectral filters, enhanced post-processing, and combination with other instruments. Nevertheless, we have shown that a micro-patterned polarization RGB detector can be the basis of an effective and compact instrument to monitor the polarization of the aurora.

Acknowledgments

The authors would like to thank Christoph Keller for the extensive comments provided to the manuscript and for the useful discussions throughout the project. The editor thanks two anonymous reviewers for their assistance in evaluating this paper.

Funding

Part of this work was funded by the NWO Synoptics TTW Perspective Program.

Conflicts of interest

The authors declare no Conflict of Interest.

Data availability statement

The data gathered for this research is formatted in the widely accepted ASDF format. Metadata includes instrument settings and a precise timestamp. All data are available upon reasonable request under the CC BY 4.0 license.

References

Astropy Collaboration, Price-Whelan AM, Lim PL, Earl N, Starkman N, et al. 2022. The Astropy Project: Sustaining and growing a community-oriented open-source project and the latest major release (v5.0) of the core package. *Astrophys J* **935**: 167. https://doi.org/10.3847/1538-4357/ac7c74.

Bagnulo S, Landolfi M, Landstreet JD, Landi Degl'Innocenti E, Fossati L, et al. 2009. Stellar spectropolarimetry with retarder waveplate and beam splitter devices. *Publ Astron Soc Pac* **121**: 993. https://doi.org/10.1086/605654.

Barthelemy M, Lamy H, Vialatte A, Johnsen MG, Cessateur G, et al. 2019. Measurement of the polarisation in the auroral N2+ 427.8 nm band. *J Space Weather Space Clim* **9**: A26. https://doi.org/10.1051/swsc/2019024.

Barthélémy M, Lilensten J, Pitout F, Simon Wedlund C, Thissen R, et al. 2011. Polarisation in the auroral red line during coordinated EISCAT Svalbard Radar/optical experiments. *Ann Geophys* **29(6)**: 1101–1112. https://doi.org/10.5194/angeo-29-1101-2011.

Bommier V, Sahal-Bréchot S, Dubau J, Cornille M. 2011. The theoretical impact polarization of the O I 6300 Å red line of Earth aurorae. *Ann Geophys* **29(1)**: 71–79. https://doi.org/10.5194/angeo-29-71-2011.

Bosse L, Lilensten J, Gillet N, Rochat S, Delboulbe A, et al. 2020. On the nightglow polarisation for space weather exploration. *J Space Weather Space Clim* **10**: 35. https://doi.org/10.1051/swsc/2020036.

Bosse L, Lilensten J, Gillet N, Brogniez C, Pujol O, et al. 2022a. At the source of the polarisation of auroral emissions: Experiments and modeling. *J Space Weather Space Clim* **12**: 7. https://doi.org/10.1051/swsc/2022004.

Bosse L, Lilensten J, Johnsen MG, Gillet N, Rochat S, et al. 2022b. The polarisation of auroral emissions: A tracer of the E region ionospheric currents. *J Space Weather Space Clim* **12**: 17. https://doi.org/10.1051/swsc/2022014.

Bourgeois S, Bosse L, Lilensten J, Gillet N, Curaba S, et al. 2022. Laboratory experiments confirm the polarization of auroral emissions. *Geophys Res Lett* **49(13)**: e2022GL098707. https://doi.org/10.1029/2022GL098707.

Burggraaff O, Schmidt N, Zamorano J, Pauly K, Pascual S, et al. 2019. Standardized spectral and radiometric calibration of consumer cameras. *Opt Express* **27**: 19,075. https://doi.org/10.1364/OE.27.019075.

Chamberlain JW. 1959. On the polarization of the oxygen red line in aurorae. *Planet Space Sci* **2(1)**: 73–75. https://doi.org/10.1016/0032-0633(59)90063-7.

Dekemper E, Vanhamel J, Kastelik J-C, Pereira N, Bolsée D, et al. 2019. New AOTF-based instrumental concepts for atmospheric science. In: *Fourteenth School on Acousto-Optics and Applications*, Grulkowski I, Linde BBJ, Duocastella M (Eds.), Vol. 25, SPIE. ISBN 978-1-5106-3183-0 978-1-5106-3184-7. https://doi.org/10.1117/12.2540981.

Donati JF, Semel M, Rees DE, Taylor K, Robinson RD. 1990. Detection of a magnetic region of HR 1099. *Astron Astrophys* **232**: L1–L4. URL https://ui.adsabs.harvard.edu/abs/1990A&A...232L...1D.

Duncan RA. 1959. Polarization of the red oxygen auroral line. *Planet Space Sci* **1(2)**: 112–IN3. https://doi.org/10.1016/0032-0633(59)90006-6.

Galand M, Chakrabarti S. 2006. Proton aurora observed from the ground. *J Atmos Sol-Terr Phys* **68(13)**: 1488–1501. https://doi.org/10.1016/j.jastp.2005.04.013.

Ginsburg VL. 1943. Polarization of lines in the night sky luminescence spectrum and in the spectrum of northern lights. In: *Doklady Akademii Nauk SSSR*, Vol. 38, pp. 237–240.

Hagen N, Stockmans T, Otani Y, Buranasiri P. 2024. Fourier-domain filtering analysis for color-polarization camera demosaicking. *Appl Opt* **63**: 2314. https://doi.org/10.1364/AO.516696.

Harang L. 1933. Eine Untersuchung der Polarisation des Nordlichtes. *Z Geophys* **9**: 162–164.

Jiang H, Fan R, Ji Y, Guo K, Xiong S, et al. 2023. Development of visible multi-bandpass filter based on F-P structure. *Coatings* **13(8)**: 1341. https://doi.org/10.3390/coatings13081341.

Lilensten J, Simon C, Barthélémy M, Moen J, Thissen R, et al. 2006. Considering the polarization of the oxygen thermospheric red line for space weather studies. *Space Weather* **4(11)**. https://doi.org/10.1029/2006SW000228.

Lilensten J, Moen J, Barthélemy M, Thissen R, Simon C, et al. 2008. Polarization in aurorae: A new dimension for space environments studies. *Geophys Res Lett* **35(8)**. https://doi.org/10.1029/2007GL033006.

Lilensten J, Barthélémy M, Amblard P-O, Lamy H, Wedlund CS, et al. 2013. The thermospheric auroral red line polarization: Confirmation of detection and first quantitative analysis. *J Space Weather Space Clim* **3**: A01. https://doi.org/10.1051/swsc/2012023.

LUCID Vision Labs I. 2018. Triton 5.0 MP Polarization Camera (Sony IMX250MZR/MYR) – LUCID. URL https://thinklucid.com/product/triton-5-mp-polarization-camera/.

Maruyama Y, Terada T, Yamazaki T, Uesaka Y, Nakamura M, et al. 2018. 3.2-MP back-illuminated polarization image sensor with four-directional air-gap wire grid and 2.5-μm pixels. *IEEE Trans Electron Devices* **65(6)**: 2544–2551. https://doi.org/10.1109/TED.2018.2829190.

Nanjo S, Nozawa S, Yamamoto M, Kawabata T, Johnsen MG, et al. 2022. An automated auroral detection system using deep learning: Real-time operation in Tromsø, Norway. *Sci Rep* **12(1)**: 8038. https://doi.org/10.1038/s41598-022-11686-8.

Peverall R, Rosén S, Peterson JR, Larsson M, Al-Khalili A, et al. 2001. Dissociative recombination and excitation of O2+: Cross sections, product yields and implications for studies of ionospheric airglows. *J Chem Phys* **114(15)**: 6679–6689. https://doi.org/10.1063/1.1349079.

Ratliff BM, Boger JK, Fetrow MP, Tyo JS, Black WT. 2006. Image processing methods to compensate for IFOV errors in microgrid imaging polarimeters. In: *Polarization: Measurement, Analysis, and Remote Sensing VII*, Vol. 6240, SPIE, pp. 106–117. https://doi.org/10.1117/12.666595.

Ratliff BM, LaCasse CF, Tyo JS. 2009. Interpolation strategies for reducing IFOV artifacts in microgrid polarimeter imagery. *Opt Express* **17(11)**: 9112–9125. https://doi.org/10.1364/OE.17.009112.

Rees MH. 1989. *Physics and Chemistry of the Upper Atmosphere* (1st edn.), Cambridge University Press. ISBN 978-0-521-32305-5 978-0-521-36848-3 978-0-511-57311-8. https://doi.org/10.1017/CBO9780511573118.

Sato T, Iijima T. 1979. Primary sources of large-scale Birkeland currents. *Space Sci Rev* **24(3)**: 347–366. https://doi.org/10.1007/BF00212423.

Shkarin A. 2022. AlexShkarin/pyLabLib: v1.4.1. https://doi.org/10.5281/zenodo.7324876.

Snik F, Keller CU. 2013. Astronomical polarimetry: Polarized views of stars and planets. In: *Planets, Stars and Stellar Systems Volume 2: Astronomical Techniques, Software, and Data*, pp. 175–221. https://doi.org/10.1007/978-94-007-5618-2_4.

Snik F, Craven-Jones J, Escuti M, Fineschi S, Harrington D, et al. 2014. An overview of polarimetric sensing techniques and technology with applications to different research fields. In: *SPIE Sensing Technology + Applications*, Chenault DB, Goldstein DH (Eds.), Vol. 90990B, SPIE. https://doi.org/10.1117/12.2053245.

Stetson PB. 1987. DAOPHOT: A computer program for crowded-field stellar photometry. *Publ Astron Soc Pac* **99**: 191. https://doi.org/10.1086/131977.

Stockmans T, Scheinowitz N, Van Der Linden E, Malysheva I, Strelow KN, et al. 2024. Sub-percent characterization and polarimetric performance analysis of commercial micropolarizer array detectors. In: *Polarization: Measurement, Analysis, and Remote Sensing XVI*, Chenault DB, Kupinski MK, Ratliff BM (Eds.), Vol. 4, SPIE. ISBN 978-1-5106-7418-9 978-1-5106-7419-6. https://doi.org/10.1117/12.3013746.

Tinbergen J. 2005. *Astronomical Polarimetry*, Cambridge University Press. ISBN 9780521018586.

Tyo JS, Goldstein DL, Chenault DB, Shaw JA. 2006. Review of passive imaging polarimetry for remote sensing applications. *Appl Opt* **45(22)**: 5453. https://doi.org/10.1364/AO.45.005453.

Tyo JS, LaCasse CF, Ratliff BM. 2009. Total elimination of sampling errors in polarization imagery obtained with integrated microgrid polarimeters. *Opt Lett* **34(20)**: 3187. https://doi.org/10.1364/OL.34.003187.

Vanhamel J, Dekemper E, Berkenbosch S, Clairquin R. 2021. Novel acousto-optical tunable filter (AOTF) based spectropolarimeter for the characterization of auroral emission. *Instrum Sci Technol* **49(3)**: 245–257. https://doi.org/10.1080/10739149.2020.1814809.

Vaughn IJ, Rodríguez-Herrera OG, Xu M, Tyo JS. 2015. A portable imaging Mueller matrix polarimeter based on a spatio-temporal modulation approach: Theory and implementation. In: *Polarization Science and Remote Sensing VII*, Vol. 9613, SPIE, pp. 961312. https://doi.org/10.1117/12.2188675.

Whiter DK, Partamies N, Gustavsson B, Kauristie K. 2023. The altitude of green OI 557.7 nm and blue $N2^+$ 427.8 nm aurora. *Ann Geophys* **41(1)**: 1–12. https://doi.org/10.5194/angeo-41-1-2023.

Cite this article as: Stockmans TA, Strelow K, Scheinowitz N, Fagginger Auer F, Mulder W, Stuik R, Cessateur G, Bosse L, Lamy H & Snik F. 2026. Conceptual design and prototyping of a three-color polarimetric imaging instrument for auroral observations. *J. Space Weather Space Clim.* **16**, 25. https://doi.org/10.1051/swsc/2026022.

Appendix A Detailed temporal progression of Stokes parameters

For every image taken, a mean q and u can be retrieved. These numbers are shown chronologically in Figures A.1 and A.2.

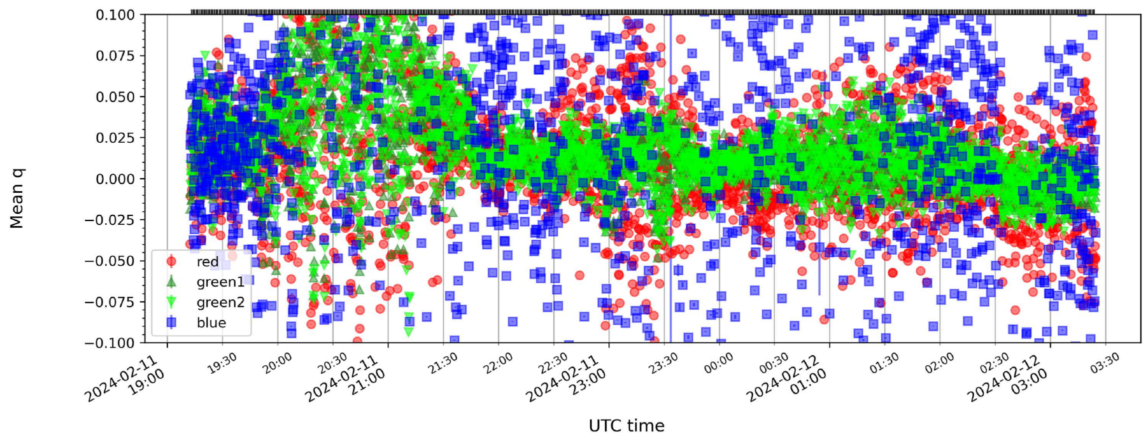

Figure A.1. Mean q over the region of interest for the same night as Figure 9.

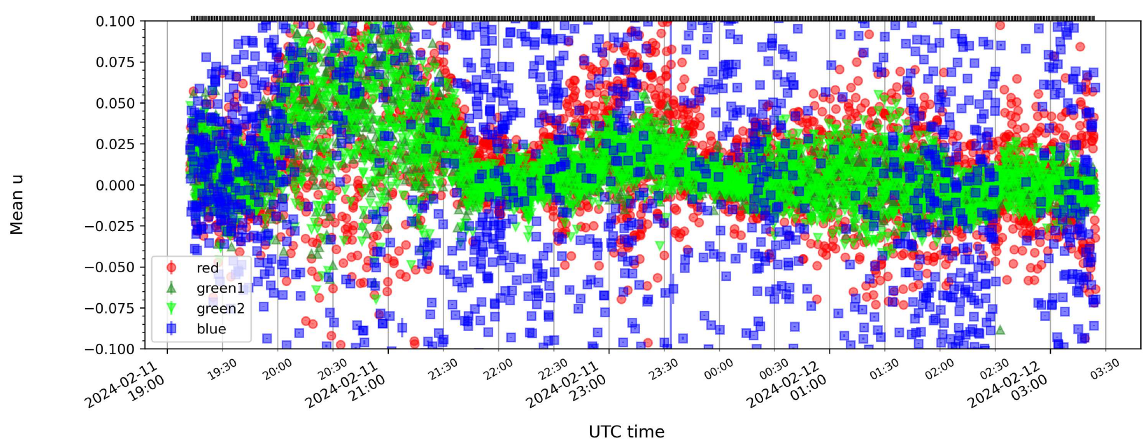

Figure A.2. Mean u over the region of interest for the same night as Figure 9.

Appendix B Relation of the dark offset to temperature

Using a heater pointed at the instrument outside of the FoV, we attempted to stabilize the temperature inside the casing and keep the motor from freezing. Figure B.1 shows the temperature of the detector over time together with the removed dark offset. As can be seen, the dark offset has been as high as one-fourth of the dynamic range of the detector. Although the temperature was only measured with 1-degree accuracy, the dark offset is estimated on a smoother scale due to the estimation of the scaling as described in Section 5.

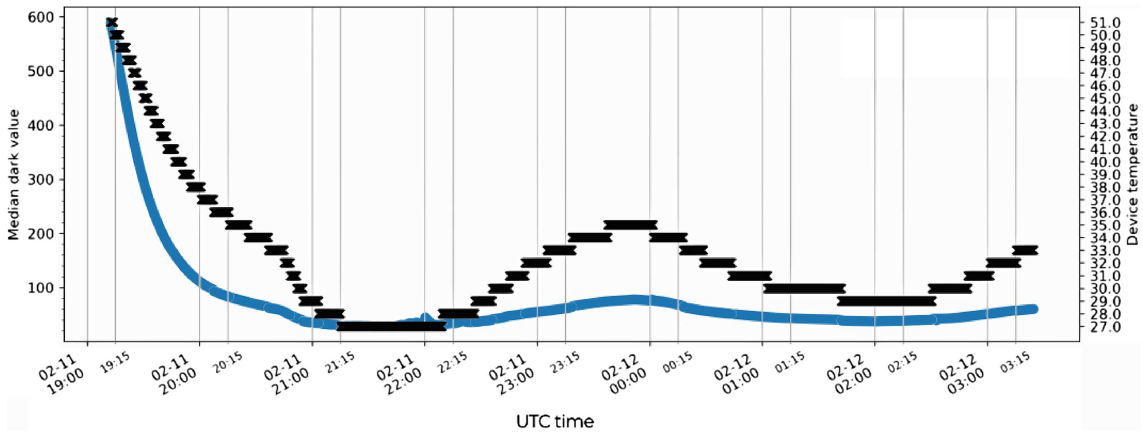

Figure B.1. Mean estimated dark value in blue and detector temperature in black, both against the UTC time.